Data Mine

Preliminary Results from a Dense Short-Period Seismic Deployment around the Source Zone of the 1886 M 7 South Carolina Earthquake

William Chen[*1], Miguel Neves[2], Qiushi Zhai[2,3], Clara Daniels[2,4], Oluwaseyifunmi Adeboboye[2], Steven Jaume[5], and Zhigang Peng[2]

Abstract

The 1886 magnitude ~7 Summerville, South Carolina, earthquake was the largest recorded on the east coast of the United States. A better understanding of this earthquake would allow for an improved evaluation of the intraplate seismic hazard in this region. However, its source fault structure remains unclear. Starting in May 2021, a temporary 19-station short-period seismic network was deployed in the Summerville region. Here, we present our scientific motivation, station geometry, and quality of the recorded seismic data. We also show preliminary results of microearthquake detections and relocations using recordings from both our temporary and four permanent stations in the region. Starting with 52 template events, including two magnitude ~3 events on 27 September 2021, we perform a matched filter detection with the one year of continuous data, resulting in a catalog of 181 total events. We then determine precise relative locations of a portion of these events using differential travel-time relocation methods, and compare the results with relocation results of 269 events from a previous seismic deployment in 2011–2012. We also determine focal mechanism solutions for three events from 27 September 2021 with magnitudes 2.0, 3.1, and 3.3, and infer their fault planes. Our relocation results show a south-striking west-dipping zone in the southern seismicity cluster, which is consistent with the thrust focal mechanism of the magnitude 3.3 earthquake on 27 September 2021 and results from the previous study based on the temporary deployment in 2011–2012. In comparison, the magnitudes 3.1 and 2.0 events likely occur on a north–south-striking right-lateral strike-slip fault further north, indicating complex patterns of stress and faulting styles in the region.

Cite this article as Chen, W., M. Neves, Q. Zhai, C. Daniels, O. Adeboboye, S. Jaume, and Z. Peng (2023). Preliminary Results from a Dense Short-Period Seismic Deployment around the Source Zone of the 1886 M 7 South Carolina Earthquake, *Seismol. Res. Lett.* **94**, 2479–2488, doi: 10.1785/0220230085.

Supplemental Material

Introduction

The 31 August 1886 magnitude (**M**) ~7 earthquake centered near Summerville, South Carolina, is the largest historical earthquake on the east coast of the United States (Nuttli *et al.*, 1986; Dutton, 1889; Neely *et al.*, 2018). Also known as the 1886 Charleston earthquake, this event caused significant damages and casualties to the nearby port city of Charleston (Bollinger, 1977; Cote, 2007), and was widely felt as far as Boston, Massachusetts, to the north and Cuba to the south. Wong *et al.* (2005) estimated that, depending on the time of day, a repeat of this earthquake today would result in up to 900 fatalities and up to $20 billion U.S. in economic losses.

Despite being located close to a major population center, the source fault of the 1886 earthquake remains unknown, mostly due to the lack of unambiguous surface rupture associated with this event (Dutton, 1889). In the past few decades, many studies have attempted to constrain its source fault based on microseismicity locations, geophysical imaging, and geomorphological and geological observations (e.g., Durá-Gómez and Talwani, 2009; Talwani and Durá-Gómez, 2009; Chapman *et al.*, 2016;

1. University of Minnesota Twin Cities, Minneapolis, Minnesota, U.S.A.; 2. School of Earth and Atmospheric Sciences, Georgia Institute of Technology, Atlanta, Georgia, U.S.A., https://orcid.org/0000-0002-8581-8551 (MN); https://orcid.org/0000-0003-2583-5146 (QZ); https://orcid.org/0009-0007-0302-1084 (OA); https://orcid.org/0000-0002-0019-9860 (ZP); 3. Now at Seismological Laboratory, California Institute of Technology, Pasadena, California, U.S.A.; 4. Now at Applied Research Associates, Burlington, Massachusetts, U.S.A.; 5. Department of Geology and Environmental Geosciences, College of Charleston, Charleston, South Carolina, U.S.A.

*Corresponding author: chen6430@umn.edu

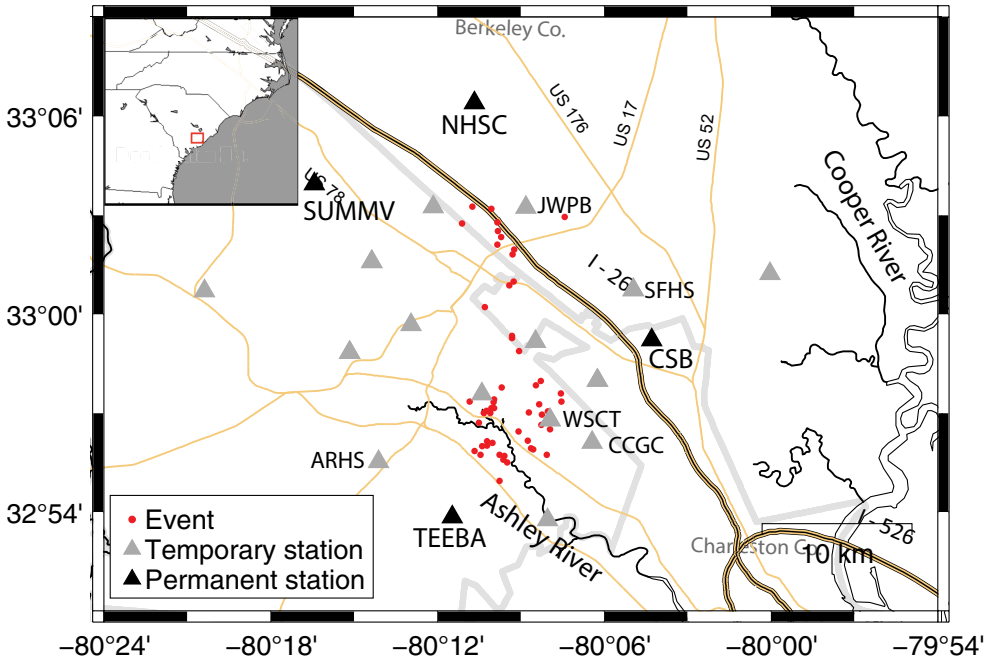

Figure 1. Map view of the study region and seismic stations. Temporary seismic stations from the YH network are represented by gray triangles, and permanent seismic stations from the US and CO networks are represented by black triangles. Events from 2021 to 2022 relocated using hypoDD are shown as red circles. Additional layers of information are same as in figure 1 of Chapman *et al.* (2016). Inset shows the study region in a larger map of the eastern United States. The color version of this figure is available only in the electronic edition.

and references therein). Pratt *et al.* (2022) recently summarized different interpretations of source faults in the Charleston–Summerville area. However, the fault structure that ruptured during the 1886 earthquake remains elusive.

Chapman *et al.* (2016) presented results from an eight-station seismic network deployed in 2011–2012 in the Middleton Place-Summerville seismic zone (MPSSZ), that is, the presumed source area of the 1886 **M** ~7 mainshock. Their relocated microseismicity mostly outlined a south-striking, west-dipping fault plane with predominately reverse motion. This observation is consistent with the well-constrained focal mechanisms from the same deployment and the general expected style of faulting and the maximum horizontal principal stress (SH_{max}) direction in this region (Lund Snee and Zoback, 2022). Chapman *et al.* (2016) also drew attention to the similarity of the modern seismicity in Summerville and surrounding areas and the 2011 **M** 5.8 Mineral, Virginia, aftershock sequence (Chapman, 2013; Meng *et al.*, 2018), both in terms of their spatial geometry and in the nature of the focal mechanisms and faulting styles.

Motivated by the recent work of Chapman *et al.* (2016), we deployed a ~20-station seismic network in the MPSSZ beginning in late May 2021. The objective of this deployment is to better define fault structures associated with modern microseismicity and to shed new insight on the fault that ruptured during the 1886 **M** ~7 earthquake. Our proposed deployment duration is two years. With double the duration and twice as many stations, as well as new techniques for detecting and relocating microseismicity, we expand on the events observed in the 2011–2012 deployment (Chapman *et al.*, 2016). In this study, we presented the station geometry and quality of data recorded by this network. In addition, we summarized preliminary results from our first year of deployment. In the next sections, we first introduced our seismic network and the recorded seismic data quality, followed by a detailed description of the detection and relocation techniques. We also examined in detail the earthquake sequence on 27 September 2021, with three events larger than **M** 2, including the largest event of **M** 3.3. Finally, we compared relocated results from a reanalysis of the 2011–2012 seismic data (Daniels, 2022) to show the similarity and difference in the microseismicity in those two time periods.

Data and Analysis Procedure

Seismic network and example waveforms

The temporary seismic network used for this study consisted of L22 three-component short-period seismometers deployed in the MPSSZ (Fig. 1) and was assigned the network code of YH. The stations were initially deployed in late May of 2021 at a sampling rate of 200 Hz; however, due to limited disk storage, the sampling rate was changed to 100 Hz since July 2021. Four permanent stations maintained by University of South Carolina (Fig. 1) were also used to supplement the data from the temporary deployment. Figure 2 shows an example field photo in the Summerville High School and the L22 short-period sensor. The recording duration and station on–off periods are shown in Dataset S1 available in the supplemental material to this article. There was a slow ramp up of the total number of operating stations in the beginning. By early October 2021, all the 19 stations were deployed.

Figure 3 shows several examples of waveforms of selected local and teleseismic earthquakes recorded by the temporary station YH.SFHS and the nearby permanent station CO.CSB. As expected, the short-period temporary stations

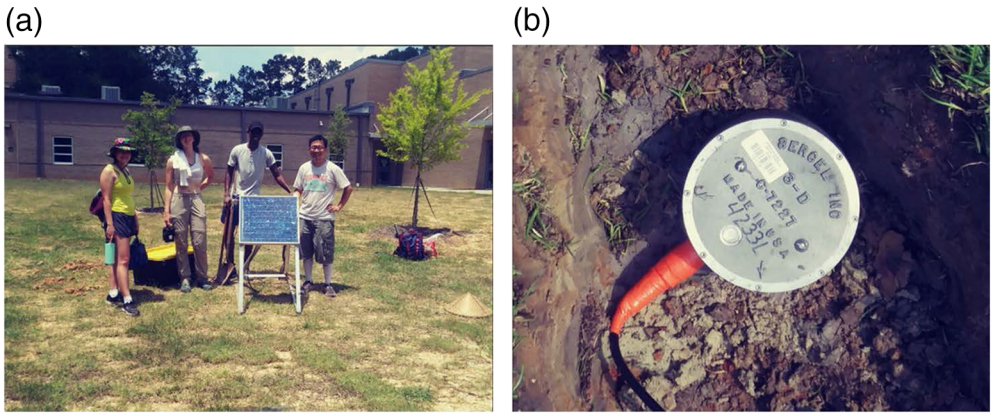

Figure 2. (a) Field installation of a seismic station in the Summerville High School (YH.SFHS) and (b) L22 short-period seismometer in position. The color version of this figure is available only in the electronic edition.

did not fully record the long-period surface waves when comparing with the broadband stations. However, their amplitude spectra are comparable in the periods shorter than 10 s.

Next, we analyzed the level of background noise levels by performing probabilistic power spectral density (PPSD) analysis (McNamara and Buland, 2004). PPSD was estimated using 1 hr long data segments (Fig. 4). The short-period seismometers show variations in noise levels in the short periods (<1 s) probably related to variations in cultural noise sources. In the long periods, high-noise levels are observed in all temporary stations (>10 s)—a phenomenon reported at various temporary deployments that has been related to poor insulation (Wilson *et al.*, 2002; Díaz *et al.*, 2010; Custódio *et al.*, 2014). In addition, the narrow corner frequency of the short-period instruments (2 Hz) makes it challenging to record long-period signals. For comparison, the noise level for the permanent broadband station CO.SUMMV remains lower than the low-noise earth model (Peterson, 1993) up to 100 s, indicating again that these permanent broadband stations perform better in long periods than the temporary short-period stations.

Matched-filter detection

Continuous waveform data were collected beginning on 26 May 2021, and 52 microseismic events were manually

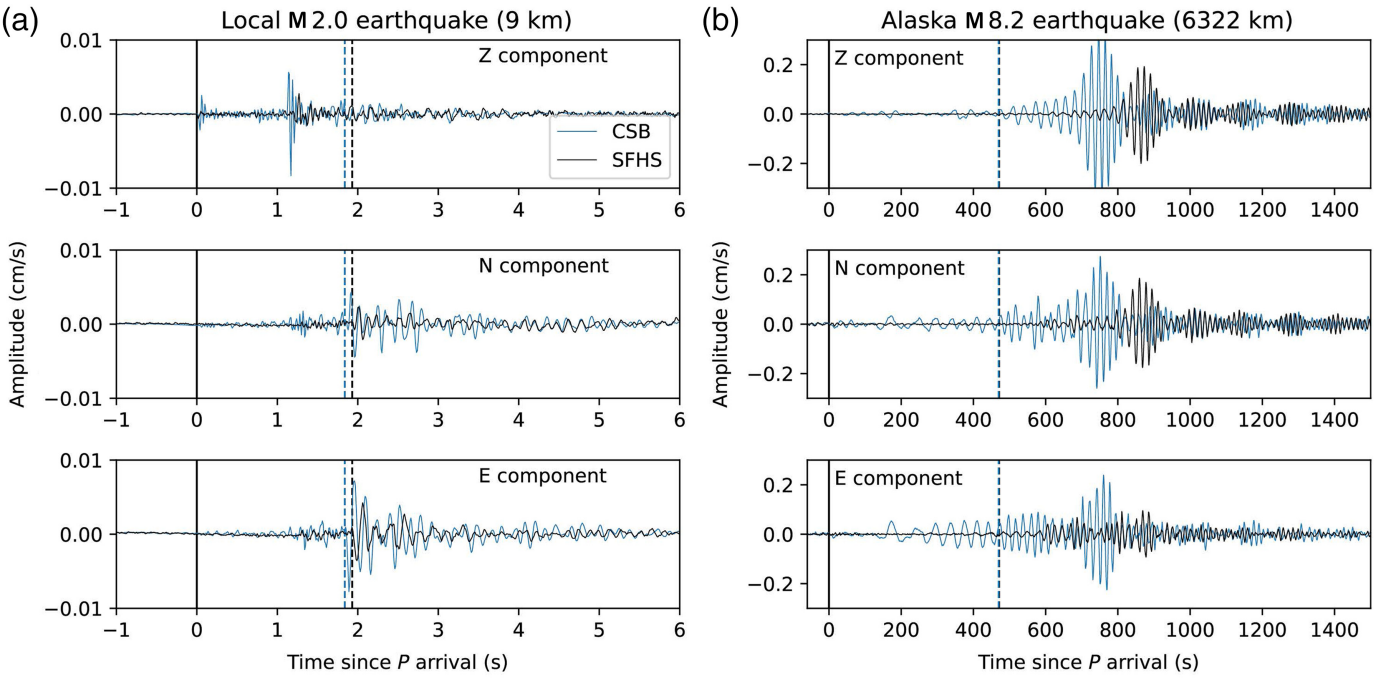

Figure 3. Comparison of waveforms recorded at a temporary station and a permanent station. (a) Three-component waveforms of a local **M** 2.0 earthquake recorded at the short-period YH.SFHS station (black) and the broadband CO.CSB station (blue). Solid black line marks the *P*-phase arrival, black dashed line marks the *S*-phase arrival at station YH.SFHS and dashed blue line at station CO.CSB. *P*-to-*S* converted phase can be observed at the vertical component (top panel). (b) Same as panel (a) but recording waveforms of the 2022 **M** 8.2 Alaska earthquake. The color version of this figure is available only in the electronic edition.

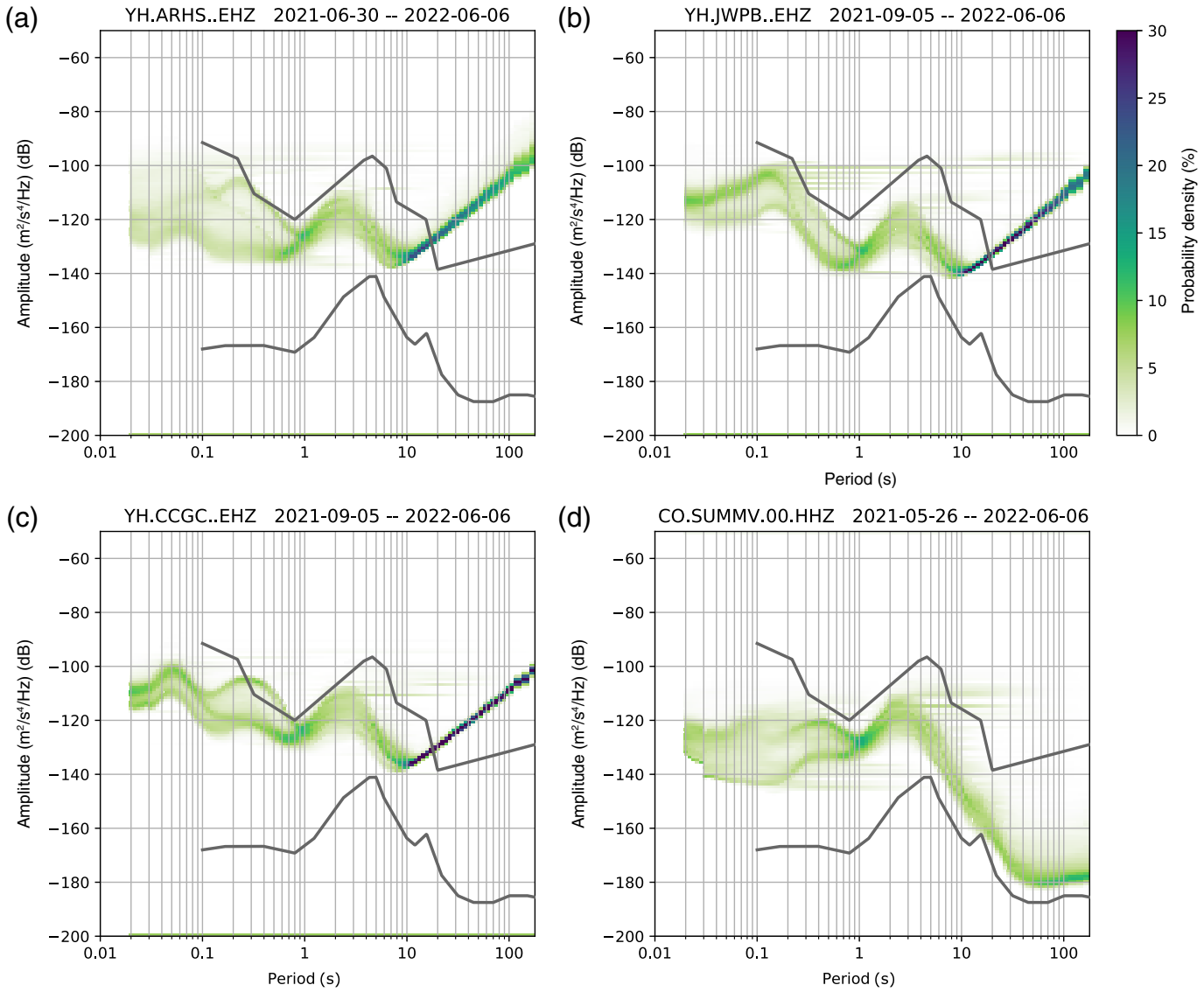

Figure 4. Probabilistic power spectral density (PPSD) analysis for stations (a) YH.ARHS, (b) YH.JWPB, (c) YH.CCGC, and (d) CO.SUMMV. Gray lines show low- and high-noise level model from Peterson (1993). The color version of this figure is available only in the electronic edition.

identified between 26 May 2021 and 6 June 2022, to be used as templates (Dataset S2) for matched-filter detection. A band-pass filter of 2–18 Hz was applied to suppress long-period seismic noises and local high-frequency noises, and the data were resampled to 40 Hz for faster template-matching computation. The signal-to-noise ratios (SNRs) of the template events were then determined based on a signal window from 0.5 s before to 3.0 s after each phase arrival and a noise window from 4.0 to 0.5 s before the phase arrival. Templates with an SNR of at least 3 on at least eight channels were used for subsequent template matching.

The template matching procedure generally followed the steps outlined in the previous studies (Peng and Zhao, 2009; Meng *et al.*, 2012; Beaucé *et al.*, 2018; Chamberlain *et al.*, 2018; Ross *et al.*, 2019; Zhai *et al.*, 2021). Cross-correlation (CC) functions were calculated between each template event and each day of continuous waveform data using the template's *P*-wave window for vertical components and *S*-wave window for horizontal components. The CC functions were then stacked and shifted to the template origin time, and the median absolute deviation (MAD) was calculated. As was done before (Peng and Zhao, 2009; Ross *et al.*, 2019), detections with a stacked CC value of at least nine times the MAD (9× MAD) and at least nine channels were compiled. Detections within two seconds of each other were identified as duplicates, and only the ones with the highest CC value were kept. Local template magnitudes were determined with $M_{Lv} = \log(A \times 2080) + \log(D) + 0.00301 \times D + 0.7$, in which A is the peak amplitude of the vertical component in millimeters, and D is the estimated distance to the

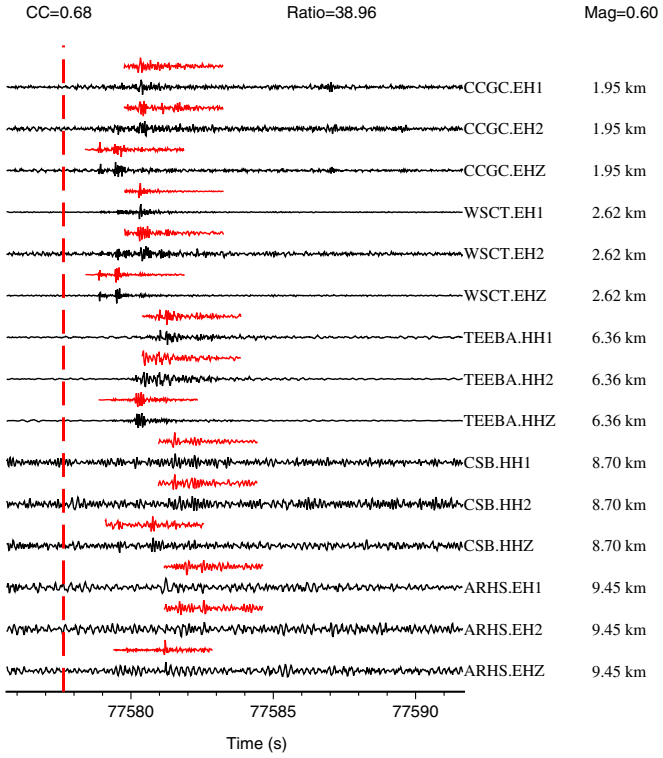

Figure 5. An example of a detection (black) from 8 September 2021 21:32:37 UTC (red dashed line), which had a magnitude of 0.60. The detection had a cross-correlation (CC) value of 0.68 with the corresponding template event (red), which occurred on 10 September 2021 03:50:04 UTC, with a magnitude of 0.40. Stations are sorted by distance from the detected event. The color version of this figure is available only in the electronic edition.

station in kilometers (Seismology Research Centre). Magnitudes of detections were estimated based on the ratio of the peak amplitudes of the detection and original template event (Peng and Zhao, 2009). We calculated this ratio for channels with a template SNR above the threshold of 3, and the median value was taken. Finally, the magnitude was calculated by assuming that an amplitude ratio of 10 corresponds to an increase in magnitude of 1 relative to the template magnitude (Peng and Zhao, 2009). These magnitudes correspond to extended local magnitudes of the templates magnitude scale (e.g., Shelly *et al.*, 2016). An example detection is shown in Figure 5. The template event occurred on 10 September 2021, at 03:50:04 UTC, with a magnitude of 0.40. The newly detected event occurred on 8 September 2021, at 21:32:37 UTC, with an estimated magnitude of 0.60. The mean CC value is 0.68, well above the 9× MAD threshold, suggesting that this is a genuine earthquake detection.

Event relocation

Prior to relocation, initial hypocenter and phase arrival times for detections were based on the best-matching template's hypocenter location. Travel-time differentials between phases of pairs of events were determined using CC of windows of 0.5 s before to 1.5 s after the *P*-phase arrival and 0.5 s before to 2.0 s after the *S*-wave arrival. The same filter as used in the detection was applied to these waveforms. To be consistent with the previous study in this region (Chapman *et al.*, 2016), we used hypoDD (Waldhauser, 2001) as our primary relocation algorithm. In addition, we also used two more relocation algorithms (XCORLOC and GrowClust) for comparison.

The hypoDD algorithm performs relocation using the double-difference method, which solves for distances between events by minimizing residuals in travel-time differences using a least-squares method (Waldhauser and Ellsworth, 2000). HypoDD allows the use of both travel-time differences derived from phase information and from CC. XCORLOC also performs differential-travel-time relocation with a grid-search algorithm but using only information derived from CCs (Lin, 2018). However, prior to performing the differential travel-time relocation, it also has an option to constrain the initial location using single-event, static station terms, and source-specific station terms (Lin, 2018). GrowClust performs relocation using only CC-derived differential travel times, also using a grid-search algorithm, but applies a hybrid clustering algorithm prior to estimating the relative locations (Trugman and Shearer, 2017).

For all three algorithms, a local velocity model from Chapman *et al.* (2016) was used (Table S1). However, hypoDD uses a set of discrete layers, whereas XCORLOC and GrowClust use an interpolated velocity gradient. The minimum CC threshold of 0.5 was used for travel-time differentials for all three algorithms. For the starting location of events for hypoDD and XCORLOC, phase arrival information was also used to provide a better estimate than the initial catalog locations. Finally, only events that are relocated using waveform CC are used in subsequent analysis.

As previously mentioned, Chapman *et al.* (2016) relocated 123 microseismic events recorded by the eight-station network from 2011 to 2012 using hypoDD. Recently, Daniels (2022) applied the matched-filter technique to the continuous waveforms from the 2011–2012 deployment and obtained a new catalog of 269 events (Dataset S3). We preprocessed waveforms of the 269 events in 2011–2012 in the same manner as the new 2021–2022 detections, and the same algorithms were then used to relocate the 2011–2012 events.

Focal mechanism solutions

Waveforms for the three **M** >2 events, from 27 September 2021, were processed by applying a 1–15 Hz band-pass filter, and cutting around the phase arrivals from −0.5 to +1.0 s for the phase window and −3.5 to −0.5 s for the noise window. We picked first-motion polarities manually and calculated the *S*-to-*P* amplitude ratio using the cut windows. We then

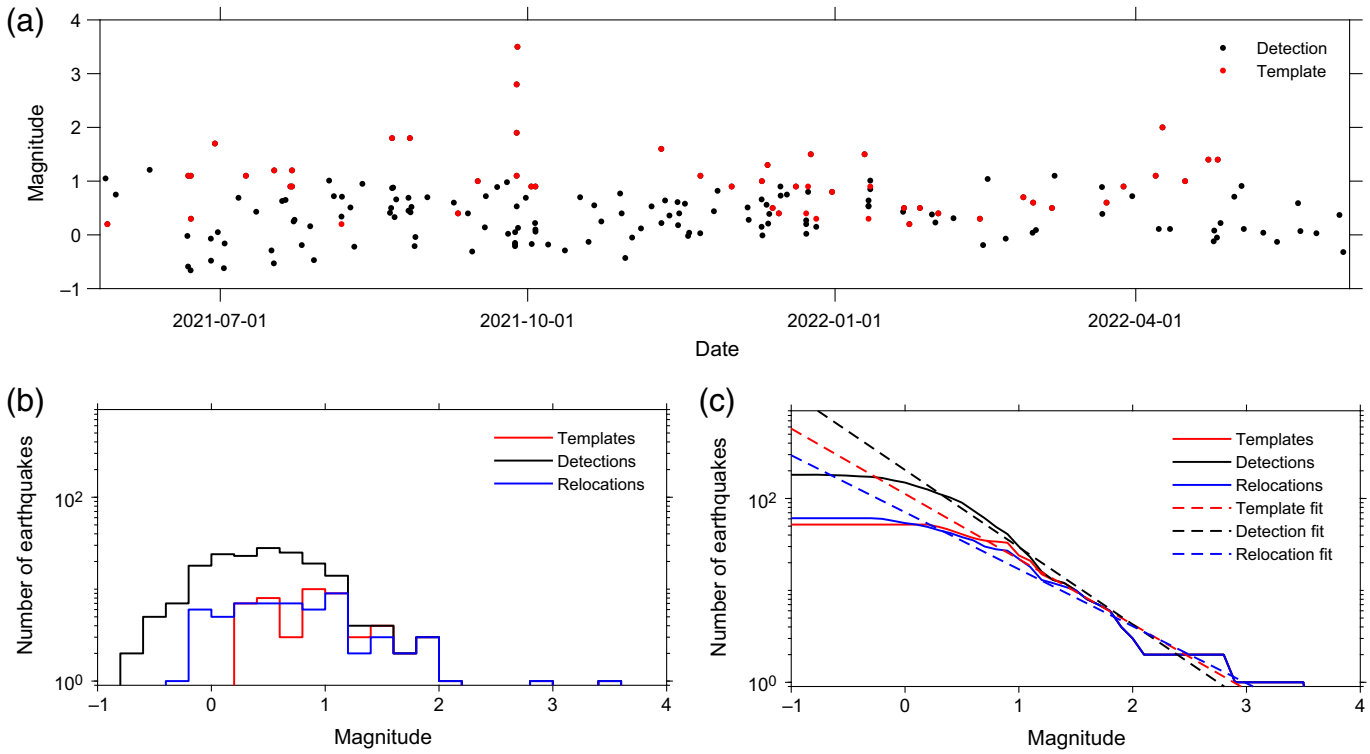

Figure 6. (a) Magnitudes of events plotted against time. The red dots represent the initial set of template events, whereas the black dots represent the detections produced by template matching. (b) Discrete numbers of events versus their magnitudes and (c) cumulative numbers of events versus their magnitudes. From the 2021–2022 events, template events are shown in red, matched-filter detections are shown in black, and events relocated by hypoDD are shown in blue. The magnitudes of completeness for the templates, detections, and relocations are 0.95, 0.55, and 0.65, respectively. Using the maximum likelihood estimate, the *b*-values of the templates, detections, and relocations are calculated to be 0.71 ± 0.17, 0.84 ± 0.15, and 0.62 ± 0.15, respectively. The Gutenberg–Richter (GR) distribution fits are plotted as dashed lines. The color version of this figure is available only in the electronic edition.

determined their focal mechanisms using the HASH program and inputting the polarities and *S*-to-*P* amplitude ratios (Hardebeck and Shearer, 2002).

Results

Detection results

Including the original 52 template events, a total of 181 events were compiled following matched-filter detection (Dataset S4) between 2021 and 2022. Notably, two **M** ~3 events along with several smaller magnitude events occurred on 27 September 2021. Figure 6 shows the magnitude–frequency distributions (MFDs) for the templates, detections, and hypoDD relocated results. MFDs are known to follow a power law distribution, commonly known as the Gutenberg–Richter (GR) relationship: $\log(N) = a - bM$, in which N is the number of earthquakes above or equal to magnitude M, and a and b are constants of the fitted line (Ishimoto and Iida, 1939; Gutenberg and Richter, 1944). But earthquake catalogs are only complete to a magnitude threshold called magnitude of completeness (M_c), above which small earthquakes are all detected and listed in that catalog. Based on the maximum curvature method (Wiemer and Wyss, 2000), we determined M_c to be 0.95, 0.55, and 0.65, for the templates, detections, and relocations catalogs, respectively. Next, we fit the MFDs above M_c to the GR relationship. Using the maximum likelihood method (Aki, 1965), we determined the *b*-values to be 0.71 ± 0.17, 0.84 ± 0.15, and 0.62 ± 0.15, for the templates, detections, and relocations, respectively (Fig. 6). Based on the lower M_c values, it is apparent that the matched-filter detection produced a higher quantity of smaller magnitude events, some of which were removed due to the applied quality thresholds used in the final relocation.

Three events occurring on 27 September 2021

Three relatively large events occurred on 27 September 2021 (Fig. 7). The first of these was a **M** 3.1 event at 16:49:14 UTC, shortly followed by an **M** 2.0 event at 16:57:19 UTC, and finally the largest, an **M** 3.3 event, occurred at 22:21:57 UTC. Based on the spatiotemporal pattern in seismicity, we consider the **M** 2.0 event to be an aftershock of the first **M** 3.1 event, as our relocation puts their epicenters at about 33 m of each other. The last **M** 3.3 event is at least 10 km away further south and hence is well beyond the aftershock zone as expected for an **M** 3.1 event (Helmstetter *et al.*, 2005). The first two smaller events occurred toward the northern end of the

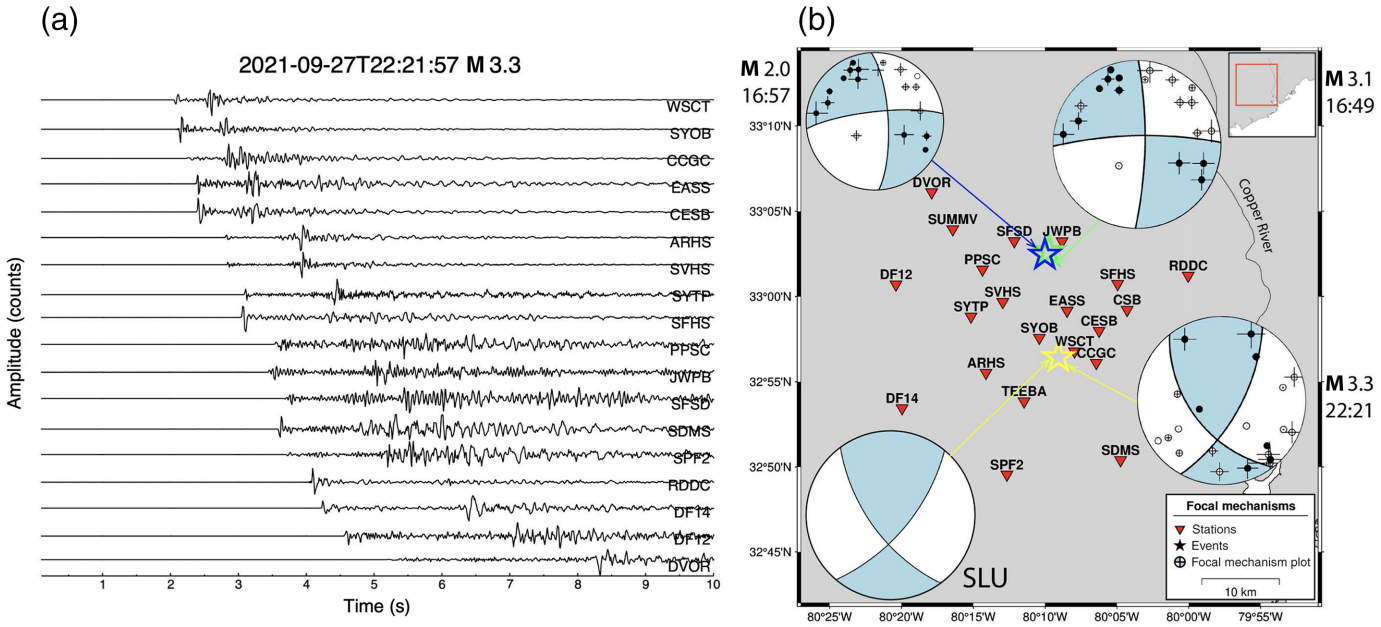

Figure 7. (a) Raw vertical component seismograms generated by the **M** 3.3 earthquake on 27 September 2021. (b) Focal mechanism solutions of the three events on 27 September 2021. Open circles represent "down" first motions, and closed circles represent "up" first motions. The magnitude ~3.1 event occurred at 16:49:14, followed by the magnitude ~2.0 event at 16:57:19, and finally the magnitude ~3.3 event at 22:21:57. The study area is outlined in red in the inset map. The color version of this figure is available only in the electronic edition.

observed seismicity and displayed strike-slip faulting, whereas the largest event occurred in the main southern cluster and displayed thrust faulting (Fig. 7b). Based on the south-striking west-dipping zone of seismicity shown subsequently, we interpret that the strike-slip events occurred on the north–south nodal plane, whereas that of the thrust event occurred on the west-dipping nodal plane.

Relocation results

Out of the 181 total detected events, 61 were relocated using hypoDD. The corresponding relocated results can be found in Dataset S5. When plotted in map view, the relocated events line up mostly in the north–south direction, and a clear west-dipping trend is visible when plotted in cross section along a N96° E-trending profile (Fig. 8). Similarly, from the 269 events in 2011–2012, an additional 97 events were relocated with hypoDD (Fig. 9). The hypoDD relocated 2011–2012 catalog can be found in Dataset S8. Movie S1 also shows the spatial distributions of seismicity from the hypoDD relocations of both the datasets with different projection directions.

One notable feature of the relocated results is a separation between events from north to south. There was a dense cluster of events toward the southern end of the seismicity with a set of sparser events toward the northern end, with the southern cluster displaying the south-striking west-dipping trend most prominently. The relocated 2021–2022 events did not display a strong west-dipping trend, with a few events seeming to contradict the trend. However, with the inclusion of the 2011–2012 events, the south-striking west-dipping trend became more prominent in the relocation results.

Relocation results of the 2021–2022 events using GrowClust and XCORLOC can be found in Datasets S6–S7, and those of the 2011–2012 events can be found in Datasets S9–S10. When compared with the hypoDD results, both the GrowClust and XCORLOC display the same overall south-striking west-dipping trend; however, it is not as well-defined. The GrowClust results also have a gap in seismicity ~3 km down-dip from the surface that is not found in the other two catalogs.

Discussion and Conclusion

The matched-filter detection performed in this study amplified the number of small-magnitude earthquakes in the catalog signified by the lower magnitude of completeness M_c and the larger b-value. The relocated catalog on the other hand shows a similar b-value to the original template catalog, whereas it still contains some new events that were not included in the initial catalog. Based on the fit of the GR relationship to the three datasets, we interpret the relocated catalog to be the most representative of the real set of earthquakes (Fig. 6). Upon plotting, the earthquakes detected and relocated in this study follow a south-striking west-dipping trend. Despite variation among the specific earthquake hypocenter results, this trend is consistent when applying all the three relocation algorithms.

When we compared the catalog produced in this study with the 2011–2012 catalog produced by Daniels (2022),

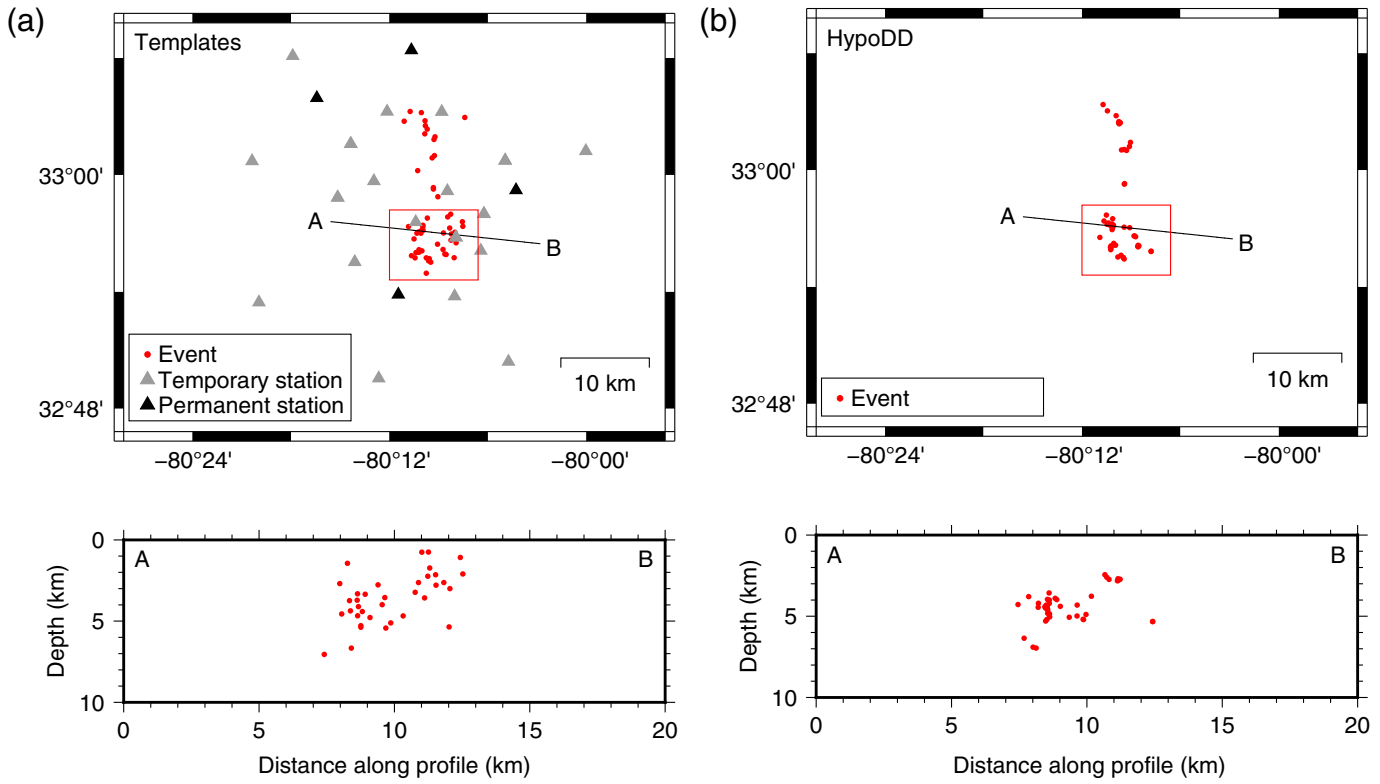

Figure 8. Map view and cross sections of (a) the 52 template event locations and (b) the 61 hypoDD relocation results. Cross sections are plotted along a N96°E-trending profile line. The color version of this figure is available only in the electronic edition.

the west-dipping trend is better defined, particularly with the hypoDD relocation results. Compared to Chapman *et al.* (2016) study, we observed a clear extension of seismicity toward north from the dipping southern cluster. The distribution of the template and hypoDD relocated catalogs shows an almost continuous distribution of shallow earthquakes further north, suggesting the presence of a north–south structure. This is consistent with the north–south-striking right-lateral strike-slip focal mechanisms for the two earthquakes on 27 September 2021, the previous focal mechanism solutions (Chapman *et al.*, 2016), and the maximum compressive stress directions in this region (Lund Snee and Zoback, 2022).

Based on these preliminary results, we demonstrated in this study the application of matched-filter detection from the recently deployed network to be a viable method for delineating relevant fault structures that host the modern seismicity. Further work is needed to develop a more complete relocated catalog to better illuminate fault structures in this region and compare with historic seismicity to better understand the source fault responsible for the 1886 ~**M** 7 earthquake. With the continuation of the YH seismic network to 2023, more seismic data will be available, and this could potentially be further supplemented by a longer-term monitoring network or a denser nodal network to increase the number of detections and more precise relocations. Application of a machine learning-based phase and polarity picker to event waveforms (Mousavi *et al.*, 2020; Zhai *et al.*, 2021) is another future direction. This would produce more events for template matching and determining focal mechanism solutions, and could allow us to better illuminate the relevant mechanisms for producing seismicity in the region.

Data and Resources

Seismic data recorded by the YH network can be downloaded from Incorporated Research Institutions for Seismology Data Management Center (IRIS DMC) at https://ds.iris.edu/mda/YH/#YH_2021-04-26_2023-03-31 (last accessed June 2022). Currently, the data are in restrictive mode and will be openly available after 2 yr of the experiment. Station YH.WSCT is openly available at IRIS DMC, and its helicorder can be viewed at http://folkworm.ceri.memphis.edu/heli_temp/ (last accessed June 2022). Most figures are generated using Generic Mapping Tools (GMT; Wessel *et al.*, 2019) and MATLAB (www.mathworks.com/products/matlab, last accessed June 2023). We use ObsPy (Beyreuther *et al.*, 2010) to make the probabilistic power spectral density (PPSD) plots in Figure 4. The earthquake catalogs compiled in this study and the respective description are included in the supplemental material.

Declaration of Competing Interests

The authors acknowledge that there are no conflicts of interest recorded.

Acknowledgments

The authors thank Derrick Murekezi, Maggie Hanley, and Steve Maloney for helping with the initial seismic deployment in 2021.

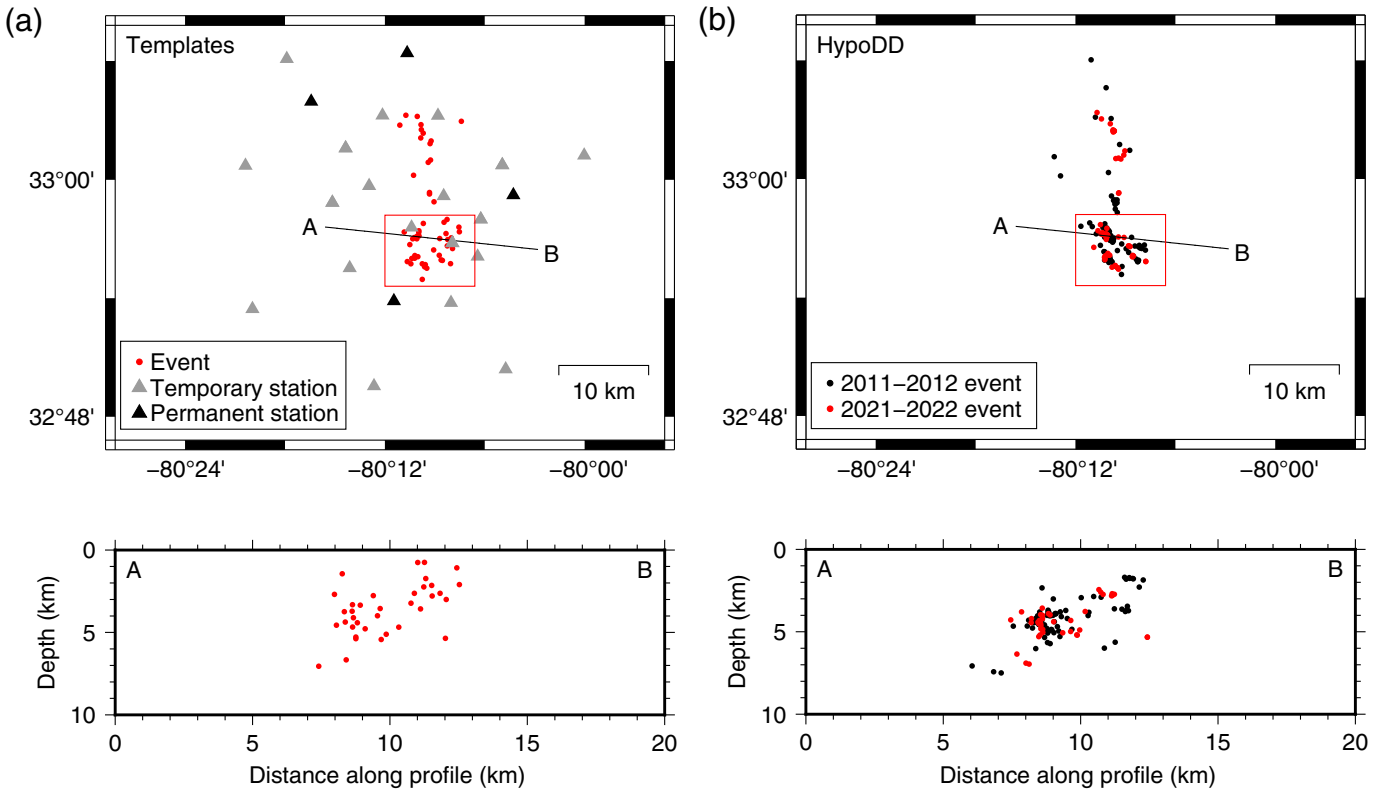

Figure 9. (a) 2021–2022 template events and (b) comparison of hypoDD relocated events from 2011 to 2012 (black) and 2021 to 2022 (red) in cross sections along a N96°E-trending profile. A 3D perspective is included in Movie S1. The color version of this figure is available only in the electronic edition.

The authors thank Martin Chapman and Qimin Wu for sharing the phase picks and relocated catalog from the 2011–2012 deployment, and information used to reproduce their figure 1 in Chapman *et al.* (2016). The authors would also like to thank many public and private owners in Summerville for allowing them to deploy seismic stations in their properties. This project is supported by U.S. Geological Survey's (USGS) National Earthquake Hazards Reduction Program (NEHRP) Grant Numbers G21AP10108 (Miguel Neves, Qiushi Zhai, Clara Daniels, and Zhigang Peng) and G21AP10093 (Steven Jaume). Miguel Neves is also supported by a Ph.D. fellowship from the Portuguese research foundation Fundação para a Ciência e a Tecnologia (FCT), Grant Number SFRH/BD/139033/2018. William Chen is supported by the Incorporated Research Institutions for Seismology (IRIS) Summer Internship program.

References

Aki, K. (1965). Maximum likelihood estimate of b in the formula log N = a – bM and its confidence limits, *Bull. Earthq. Res. Inst. Tokyo Univ.* **43,** 237–239.

Beaucé, E., W. B. Frank, and A. Romanenko (2018). Fast matched filter (FMF): An efficient seismic matched-filter search for both CPU and GPU architectures, *Seismol. Res. Lett.* **89,** no. 1, 165–172, doi: 10.1785/0220170181.

Beyreuther, M., R. Barsch, L. Krischer, T. Megies, Y. Behr, and J. Wassermann (2010). ObsPy: A Python toolbox for seismology, *Seismol. Res. Lett.* **81,** no. 3, 530–533.

Bollinger, G. A. (1977). Reinterpretation of the intensity data for the 1886 Charleston, South Carolina, earthquake, in studies related to the Charleston, South Carolina earthquake of 1886: A preliminary report, *U.S. Geol. Surv. Profess. Pap. 1028*, D. W. Rankin (Editor), 17–32, doi: 10.3133/pp1028.

Chamberlain, C. J., C. J. Hopp, C. M. Boese, E. Warren-Smith, D. Chambers, S. X. Chu, K. Michailos, and J. Townend (2018). Eqcorrscan: Repeating and near-repeating earthquake detection and analysis in python, *Seismol. Res. Lett.* **89,** no. 1, 173–181, doi: 10.1785/0220170151.

Chapman, M. C. (2013). On the rupture process of the 23 August 2011 Virginia earthquake, *Bull. Seismol. Soc. Am.* **103,** 613–628, doi: 10.1785/0120120229.

Chapman, M. C., J. N. Beale, A. C. Hardy, and Q. Wu (2016). Modern seismicity and the fault responsible for the 1886 Charleston, South Carolina, earthquake, *Bull. Seismol. Soc. Am.* **106,** 364–372, doi: 10.1785/0120000006.

Cote, R. M. (2007). *City of Heroes: The Great Charleston Earthquake of 1886*, Corinthian Books, Mt. Pleasant, South Carolina.

Custódio, S., N. A. Dias, B. Caldeira, F. Carrilho, S. Carvalho, C. Corela, J. Díaz, J. Narciso, G. Madureira, L. Matias, *et al.* (2014). Ambient noise recorded by a dense broadband seismic deployment in western Iberia, *Bull. Seismol. Soc. Am.* **104,** no. 6, 2985–3007.

Daniels, C. (2022). Improved understanding of intraplate earthquakes in the Southeastern USA with Matched filter detection, *Ph.D. Thesis*, Georgia Tech, July 2022, available at https://smartech.gatech.edu/handle/1853/67303 (last accessed June 2022).

Díaz, J., A. Villaseñor, J. Morales, A. Pazos, D. Córdoba, J. Pulgar, J. L. García-Lobón, M. Harnafi, R. Carbonell, J. Gallart, *et al.* (2010). Background noise characteristics at the IberArray broadband seismic network, *Bull. Seismol. Soc. Am.* **100,** no. 2, 618–628.

Durá-Gómez, I., and P. Talwani (2009). Finding faults in the Charleston Area, South Carolina: 1. Seismological data, *Seismol. Res. Lett.* **80,** 883–900, doi: 10.1785/gssrl.80.5.883.

Dutton, C. E. (1889). The Charleston earthquake of August 31, 1886, *Ninth Annual Report of the U.S. Geol. Surv.*, U.S. Gov. Printing Office, Washington, D.C., 203–528.

Gutenberg, B., and C. F. Richter (1944). Frequency of earthquakes in California, *Bull. Seismol. Soc. Am.* **34,** no. 4, 185–188, doi: 10.1785/bssa0340040185.

Hardebeck, J. L., and P. M. Shearer (2002). A new method for determining first-motion focal mechanisms, *Bull. Seismol. Soc. Am.* **92,** no. 6, 2264–2276, doi: 10.1785/0120010200.

Helmstetter, A., Y. Y. Kagan, and D. D. Jackson (2005). Importance of small earthquakes for stress transfers and earthquake triggering, *J. Geophys. Res.* **110,** no. B5, doi: 10.1029/2004JB003286.

Ishimoto, M., and K. Iida (1939). Observations of earthquakes registered with the microseismograph constructed recently, *Bull. Earthq. Res. Inst.* **17,** 443–478.

Lin, G. (2018). The source-specific station term and waveform cross-correlation earthquake location package and its applications to California and New Zealand, *Seismol. Res. Lett.* **89,** 1877–1885, doi: 10.1785/0220180108.

Lund Snee, J., and M. D. Zoback (2022). State of stress in areas of active unconventional oil and gas development in North America, *AAPG Bull.* **106,** 355–385, doi: 10.1306/08102120151.

McNamara, D. E., and R. P. Buland (2004). Ambient noise levels in the continental United States, *Bull. Seismol. Soc. Am.* **94,** no. 4, 1517–1527, doi: 10.1785/012003001.

Meng, X., H. Yang, and Z. Peng (2018). Foreshocks, b value map, and aftershock triggering for the 2011 Mw 5.7 Virginia earthquake, *J. Geophys. Res.* **123,** 5082–5098, doi: 10.1029/2017JB015136.

Meng, X., X. Yu, Z. Peng, and B. Hong (2012). Detecting earthquakes around Salton Sea following the 2010 M_w 7.2 El Mayor-Cucapah earthquake using GPU parallel computing, *Procedia Comput. Sci.* **9,** 937–946, doi: 10.1016/j.procs.2012.04.100.

Mousavi, S. M., W. L. Ellsworth, W. Zhu, L. Y. Chuang, and G. C. Beroza (2020). Earthquake transformer—An attentive deep-learning model for simultaneous earthquake detection and phase picking, *Nat. Commun.* **11,** 3952, doi: 10.1038/s41467-020-17591-w.

Neely, J., S. Stein, M. Merino, and J. Adams (2018). Have we seen the largest earthquakes in eastern North America? *Phys. Earth Plan. In.* **284,** 17–27, doi: 10.1016/j.pepi.2018.09.005.

Nuttli, O. W., G. A. Bollinger, and R. B. Herrmann (1986). The 1886 Charleston, South Carolina, earthquake—A 1986 perspective, *U.S. Geol. Surv. Circ. 985*, doi: 10.3133/cir985.

Peng, Z., and P. Zhao (2009). Migration of early aftershocks following the 2004 Parkfield earthquake, *Nature Geosci.* **2,** 877–881, doi: 10.1038/ngeo697.

Peterson, J. (1993). Observations and modeling of seismic background noise, *U.S. Geol. Surv. Open-File Rept. 93-322*, doi: 10.3133/ofr93322.

Pratt, T. L., A. K. Shah, R. C. Counts, J. W. Horton, and M. C. Chapman (2022). Shallow faulting and folding in the epicentral area of the 1886 Charleston, South Carolina, earthquake, *Bull. Seismol. Soc. Am.* **112,** no. 4, 2097–2123, doi: 10.1785/0120210329.

Ross, Z. E., B. Idini, Z. Jia, O. L. Stephenson, M. Zhong, X. Wang, Z. Zhan, M. Simons, E. J. Fielding, S. Yun, *et al.* (2019). Hierarchical interlocked orthogonal faulting in the 2019 Ridgecrest earthquake sequence, *Science* **366,** 346–351, doi: 10.1126/science.aaz0109.

Seismology Research Centre (2021). Waves: Product user manual, Richmond, VIC Australia, available at https://www.src.com.au/downloads/waves/ (last accessed June 2023).

Shelly, D. R., W. L. Ellsworth, and D. P. Hill (2016). Fluid-faulting evolution in high definition: Connecting fault structure and frequency-magnitude variations during the 2014 Long Valley Caldera, California, earthquake swarm, *J. Geophys. Res.* **121,** no. 3, 1776–1795, doi: 10.1002/2015JB012719.

Talwani, P., and I. Durá-Gómez (2009). Finding faults in the Charleston Area, South Carolina: 2. Complementary data, *Seismol. Res. Lett.* **80,** 901–919, doi: 10.1785/gssrl.80.5.901.

Trugman, D. T., and P. M. Shearer (2017). GrowClust: A hierarchical clustering algorithm for relative earthquake relocation, with application to the Spanish springs and Sheldon, Nevada, earthquake sequences, *Seismol. Res. Lett.* **88,** 379–391, doi: 10.1785/0220160188.

Waldhauser, F. (2001). HypoDD: A computer program to compute double-difference earthquake locations, *USGS Open File Rep. 01-113.*

Waldhauser, F., and W. L. Ellsworth (2000). A double-difference earthquake location algorithm: Method and application to the northern Hayward fault, *Bull. Seismol. Soc. Am.* **90,** 1353–1368, doi: 10.1785/0120000006.

Wessel, P., J. F. Luis, L. Uieda, R. Scharroo, F. Wobbe, W. H. F. Smith, and D. Tian (2019). The generic mapping tools version 6, *Geochem. Geophys. Geosys.* **20,** 5556–5564, doi: 10.1029/2019GC008515

Wiemer, S., and M. Wyss (2000). Minimum magnitude of completeness in earthquake catalogs: Examples from Alaska, the Western United States, and Japan, *Bull. Seismol. Soc. Am.* **90,** no. 4, 859–869, doi: 10.1785/0119990114.

Wilson, D., J. Leon, R. Aster, J Ni, J. Schlue, S. Grand, S. Semken, S. Baldridge, and W. Gao (2002). Broadband seismic background noise at temporary seismic stations observed on a regional scale in the southwestern United States, *Bull. Seismol. Soc. Am.* **92,** no. 8, 3335–3342.

Wong, I., J. Bouabid, W. Graf, C. Huyck, A. Porush, W. Silva, T. Siegel, G. Bureau, R. Eguchi, and J. Knight (2005). Potential losses in a repeat of the 1886 Charleston, South Carolina, earthquake, *Earthq. Spectra* **21,** no. 4, 1157–1184, doi: 10.1193/1.2083907.

Zhai, Q., Z. Peng, L. Y. Chuang, Y.-M. Wu, Y.-J. Hsu, and S. Wdowinski (2021). Investigating the impacts of a wet typhoon on microseismicity: A case study of the 2009 typhoon Morakot in Taiwan based on a template matching catalog, *J. Geophys. Res.* **126,** e2021JB023026, doi: 10.1029/2021JB023026.

Manuscript received 14 March 2023
Published online 18 July 2023